Lawrence Berkeley National Laboratory
LBL Publications

Title
Advantages of a variable-resolution global climate model in reproducing the seasonal evolution of East Asian summer monsoon

Permalink
https://escholarship.org/uc/item/46s0r598

Journal
International Journal of Climatology, 43(1)

ISSN
0899-8418

Authors
Zhu, Haonan
Zhang, Jie
Xu, Zexuan
et al.

Publication Date
2023

DOI
10.1002/joc.7796

Peer reviewed

RESEARCH ARTICLE

Advantages of a variable-resolution global climate model in reproducing the seasonal evolution of East Asian summer monsoon

Haonan Zhu[1] | Jie Zhang[2,3] | Zexuan Xu[4] | Alan V. Di Vittorio[4] | Xiaoge Xin[2,3] | Chan Xiao[5] | Yonghua Li[1]

[1]Chongqing Climate Center, Chongqing, China

[2]CMA Earth System Modeling and Prediction Centre, Beijing, China

[3]State Key Laboratory of Severe Weather, Beijing, China

[4]Climate and Ecosystem Science Division, Lawerence Berkeley National Laboratory, Berkeley, California, USA

[5]Beijing Climate Center, China Meteorological Administration, Beijing, China

Correspondence
Jie Zhang, CMA Earth System Modeling and Prediction Centre, 46, Zhongguancun Nandajie, Haidian District, Beijing 100081, China.
Email: jiezhang@cma.gov.cn

Funding information
National Key Research and Development Program of China CERC-WET Project, Grant/Award Number: 2018YFE0196000; U.S. Department of Energy, Office of Science, Office of International Affairs, U.S./China Clean Energy Research Center - Water/Energy Technologies (CERC-WET) project, Grant/Award Number: DE-IA0000018

Abstract

The East Asian summer monsoon (EASM) is unique among monsoon systems that it features meridional evolution of the summer monsoon. In this study, we evaluate the performances of a Variable-Resolution Community Earth System Model (VR-CESM) regionally refined over eastern China (14 km) in reproducing the seasonal evolution of EASM precipitation over China. Compared with reference datasets, VR-CESM shows better performance than the corresponding globally uniform coarse-resolution model CESM (quasi-uniform 1°), especially over western China where complex local topography exists. The northward monsoon migration is closely related to low-level southerly flows and vertical moisture advection, which are more reasonably simulated in VR-CESM. The four critical timings of the EASM (monsoon onset, withdrawal, peak, and duration) are also better captured in VR-CESM than in CESM. The corresponding spatial Pearson correlation coefficients of the four critical timings with respect to reference datasets are about 0.1 higher in VR-CESM than those in CESM. Both models are most accurate in simulating monsoon onset and least accurate at simulating the monsoon peak. The overestimated zonal thermal contrast in CESM is responsible for the earlier monsoon onset and excessive precipitation in September over the Yangtze River valley. Finer resolution in VR-CESM, especially over the Tibetan Plateau (TP), appears to be a main factor in simulating better zonal thermal contrast and seasonal evolution of the EASM.

KEYWORDS

East Asian summer monsoon, low-level circulation, resolution, seasonal evolution, thermal contrast, VR-CESM

1 | INTRODUCTION

East Asian summer monsoon (EASM) usually starts in late April over northern Indochina, propagates north of the South China Sea, and then advances northward to north China, Korean Peninsula, and Japan. It brings a humid climate and torrential rainfall to East Asia and significantly impacts local agricultural productivity, socio-economic development, and approximately one-third of the world's population (Chen *et al.*, 2015). EASM is a very complex system including interactive processes between mid-latitude and tropical origins (Zhou *et al.*, 2018), both dynamical and thermal forcing over the Tibetan Plateau (Wu *et al.*, 2007; Chen and Bordoni, 2014), and influences from human activities (Zhang, 2015). Due to the complexity of physical processes and interactions, EASM simulation, especially its temporal evolution, is still a big challenge for the models in phase 6 of Coupled Model Intercomparison Project (CMIP6; Xin *et al.*, 2020; Yan *et al.*, 2021).

Previous studies indicate that horizontal resolution is critical to monsoon simulation. Models with finer horizontal resolution consistently improve precipitation characteristics, including more accurate orographic rainfall, more reasonable seasonal climate, and characterization of small-scale features (Kitoh and Kusunoki, 2008; Ogata *et al.*, 2017; Zhang *et al.*, 2018). Huang *et al.* (2018) evaluated the global summer precipitation simulated by 23 fine- and coarse-resolution CMIP5 models. They found that fine-resolution models outperform coarse-resolution models in reproducing summer precipitation over most continents, which is partially due to the more detailed terrain and land covers. Model resolutions in CMIP6 are finer than in CMIP5 models and may also be responsible for improvements in the annual cycle of precipitation and the spatial distribution of extreme precipitation in the western North Pacific and East Asia (Chen *et al.*, 2021). However, due to the limitation of computational resources, horizontal resolutions of most global climate models are relatively coarse, which leads to significant biases in mountain precipitation due to heavily smoothed and inaccurately represented topographic features (Xu *et al.*, 2018).

Variable-resolution global climate models are global models with user-defined regions of fine resolution directly embedded in a coarser global grid. The refined grid includes transitional buffers that step gradually from the coarse outer-domain resolution to the fine inner-domain resolution. A variable-resolution model with unstructured grids has fewer artefacts at the boundaries than regional climate models, which suffer from truncation errors in the transition zone due to resolution inconsistencies with driving fields at the boundary (Ringler *et al.*, 2011; Syed *et al.*, 2014; Cha *et al.*, 2016). With much fewer grid cells than fine resolution over the entire globe, a variable-resolution model can produce reasonable, fine-resolution results on regional domains with reduced computational cost. Gibelin and Déqué (2003) showed that a variable-resolution model could realistically reproduce the Mediterranean region's main climate characteristics. Zou *et al.* (2010) demonstrated that variable-resolution models could be useful for rainfall variability simulation over eastern China.

The variable-resolution Community Earth System Model (VR-CESM) is a special configuration of the Community Earth System Model (CESM). VR-CESM has the potential to improve regional climate simulation at fine resolution without adversely impacting the mean global circulation (Zarzycki *et al.*, 2015; Rhoades *et al.*, 2016). A marine air penetration event study suggested that the synoptic-scale meteorological pattern in California can be reasonably reproduced by VR-CESM (Wang and Ullrich, 2018). The simulated monthly climatology and spatial pattern of local wind fields are also consistent with observations (Wang *et al.*, 2018). Compared with uniform-resolution models, VR-CESM better captures the spatial patterns of temperature, precipitation, and snowpack in the Rocky Mountains (Wu *et al.*, 2017) and more accurately simulate seasonal climate across the Tibetan Plateau and complex terrains (Rahimi *et al.*, 2019). Xu *et al.* (2021) further evaluated VR-CESM with respect to the major hydroclimate variables in the western United States and eastern China and concluded that VR-CESM outperforms CESM and other RCMs. Overall, previous studies of VR-CESM have found that VR-CESM simulates precipitation well in the areas of refined resolution.

In this study, the seasonal progression of the EASM over eastern China is examined with a VR-CESM simulation with 1/8° refined resolution over eastern China. This simulation also has the same refined resolution over the western United States and 1° resolution elsewhere. The same global model at a quasi-uniform 1° resolution, referred as CESM in this paper, is also employed to examine the differences due to refining resolution. The rest of the paper is organized as follows. Section 2 briefly introduces the model, data, and methods. Model performance in reproducing the seasonal evolution of EASM is evaluated in section 3. Relative monsoon circulations and land–sea thermal contrasts are also examined in section 3. Finally, highlights of the findings are summarized in section 4.

2 | MODEL, DATA, AND METHOD

2.1 | CESM and VR-CESM

Version 1.5.5 of CESM is used in this study. The model uses a globally uniform grid modelling framework and is

managed by the National Center for Atmospheric Research, Boulder, CO. CESM uses the Community Atmosphere Model version 5 (CAM5; Gettelman *et al.*, 2018) with the Spectral Element dynamical core (CAM5-SE) and the Community Land Model with Satellite Phenology version 4.0 (CLM4-SP; Zarzycki and Jablonowski, 2014). The prognostic Morrison-Gettelman microphysics scheme is employed and helps to improve representation of the mixed-phase clouds (Gettelman *et al.*, 2015). The shallow convection scheme and the deep convection scheme were developed by Park and Bretherton (2009) and Zhang and McFarlane (1995), respectively. The horizontal resolution is about 1° uniformly in the CESM, and also outside of the refined-resolution regions in the VR-CESM.

VR-CESM is a variable-resolution version of CESM. Model mesh is refined over the four major river basins in

eastern China (i.e., the Yangzte River, Yellow River, Hai River, and China Coastal watersheds) with a horizontal resolution of about 1/8°, approximately 14 km (Figure 1a). The resolution outside the focus regions includes transitional buffers from 1/4°, 1/2° to 1°, with the Tibetan Plateau (TP) in a buffer having approximately 28 km resolution. Model grids over the five major watersheds in the western United States (i.e., the Upper and Lower Colorado River watershed, the Great Basin watershed, the Columbia River watershed, and the California watershed) are also refined to 1/8° during the global simulation, but we do not address this region in this study. The variable-resolution cubed-sphere mesh was generated by the software package SQuadGen (Ullrich, 2014). The land topography used in the model was derived from a resolution-dependent smoothing of a global 30 arc sec elevation United States Geological Survey (USGS)

(a) **Eastern China**

(b)
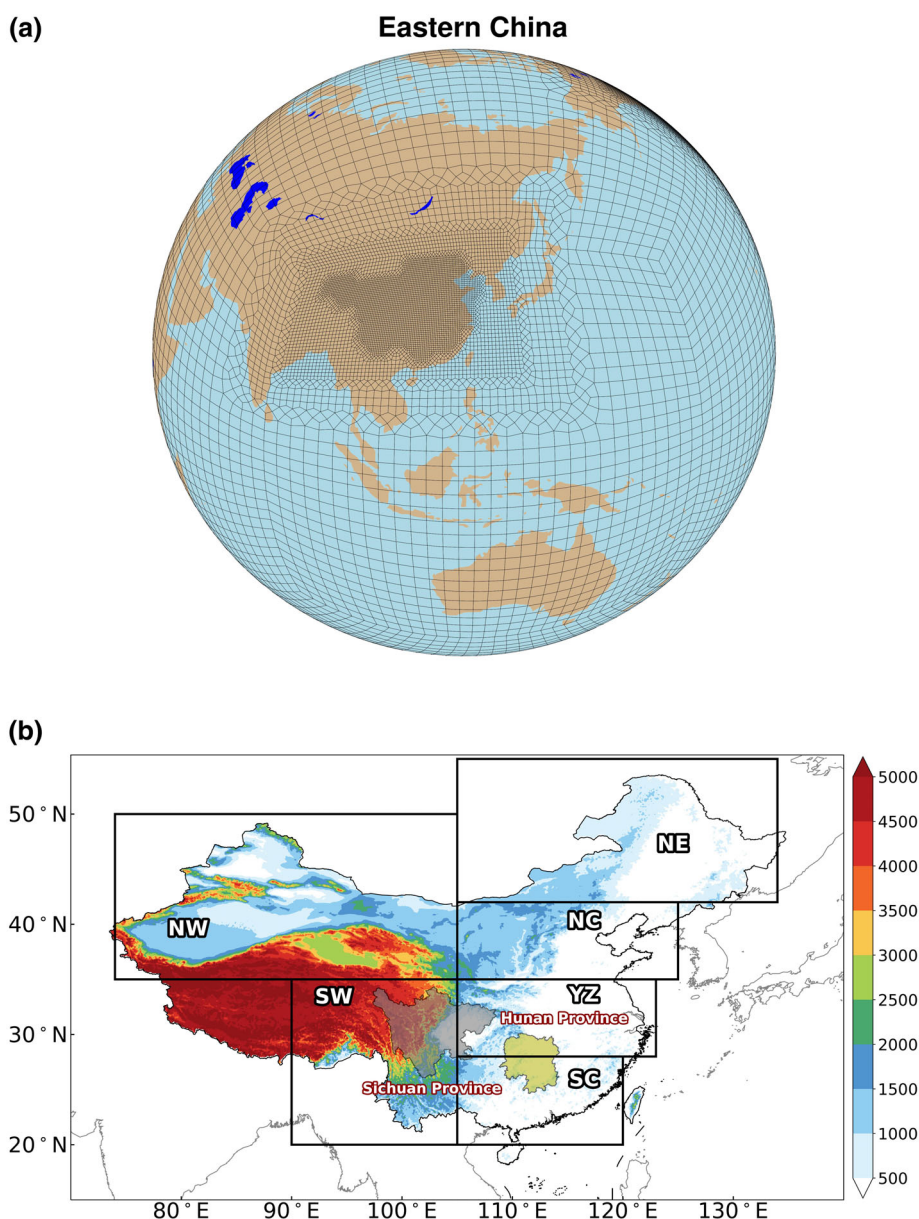
**FIGURE 1** (a) Schematic representation of the refined model grid in VR-CESM over eastern China. Modified from Xu *et al.* (2021). The resolution grid varies from 14 to 55 km. (b) Topography over China (shaded, units: m). Black rectangles mark the six subregions of China: northwest China (NW, 35°–50°N, 74°–105°E), southwest China (SW, 20°–35°N, 90°–105°E), northeast China (NE, 42°–55°N, 105°–134°E), north China (NC, 35°–42°N, 105°–125°E), Yangtze River valley (YZ, 28°–35°N, 105°–123°E), and south China (SC, 20°–28°N, 105°–120°E). The semitransparent polygons denote the Sichuan province and Hunan province [Colour figure can be viewed at wileyonlinelibrary.com]

dataset (GTOPO30) using methods outlined in Zarzycki *et al.* (2015). Model information and grid setting are detailed in Xu *et al.* (2021).

We have performed two identical simulations with VR-CESM and CESM with the Atmospheric Model Intercomparison Protocols component set (Gates, 1992). The historical simulations were run from 1969 to 2006.

Twenty-eight years from 1979 to 2006 are evaluated. The daily outputs of precipitation, zonal and meridional wind at 850, 500, and 200 hPa (U850&V850, U500&V500, U200&V200), and air temperature at 500 hPa (T500) are analysed. Meanwhile, vertical velocity (ω_{500}), specific humidity at 850 hPa (q_{850}), and evapotranspiration are used to calculate moisture budget.
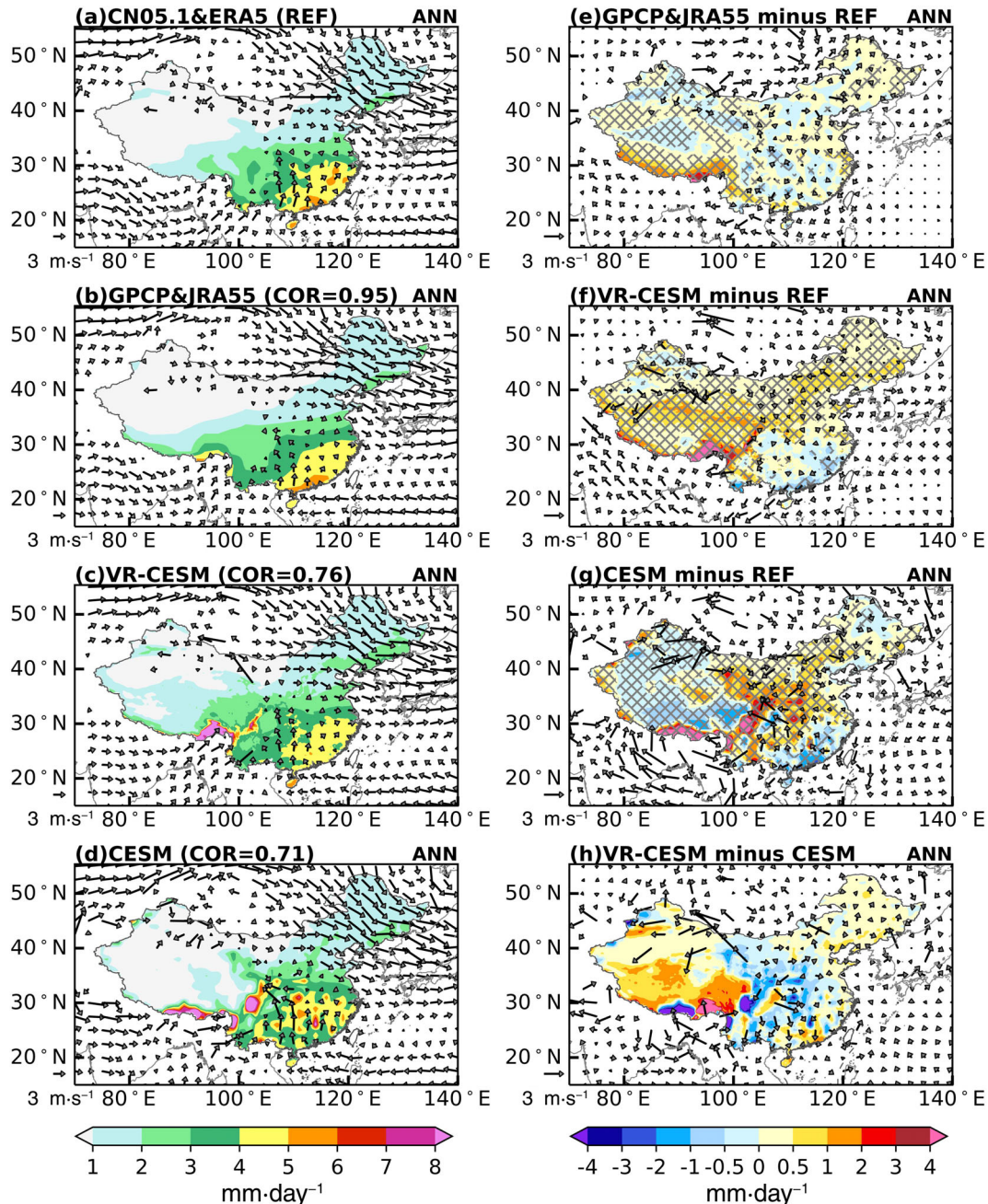
FIGURE 2 Annual mean precipitation (shaded, units: mm·day^{-1}) and 850 hPa horizontal wind (vectors, units: m·s^{-1}) over East Asia in (a) CN05.1 and ERA5 (reference), (b) GPCP and JRA55, (c) VR-CESM, and (d) CESM. COR in (b–d) stand for the spatial correlation with the CN05.1 precipitation. The differences of (b–d) against (a) are shown in (e–g), respectively. (h) The differences between VR-CESM and CESM. The hatched area in (e–h) represents the precipitation biases relative to CN05.1 exceeding the 95% confidence level based on Student's *t* test [Colour figure can be viewed at wileyonlinelibrary.com]

FIGURE 3 Same as Figure 2, but for the results in June–July–August (JJA) [Colour figure can be viewed at wileyonlinelibrary.com]
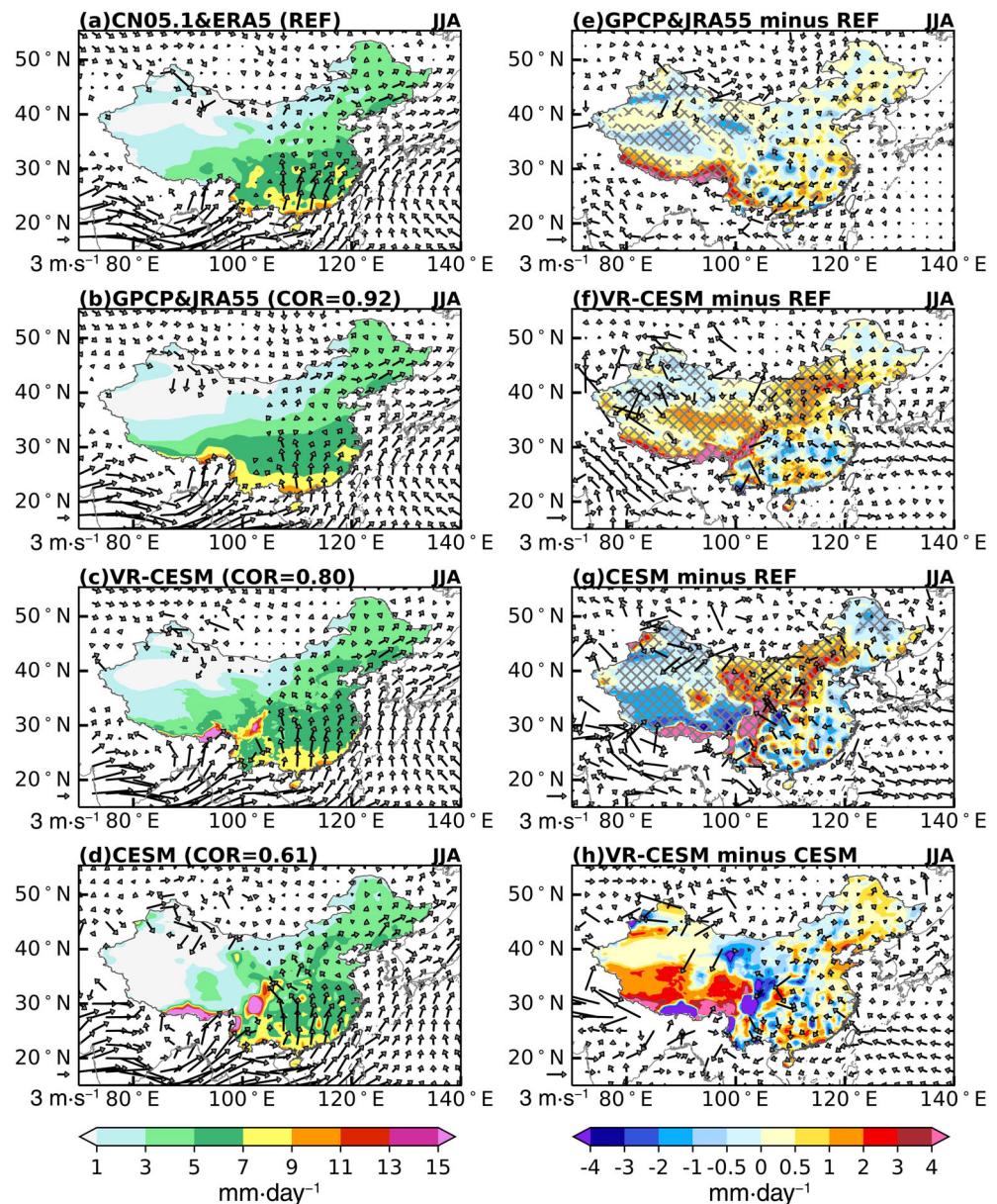
2.2 | Data

Two precipitation datasets and two reanalysis datasets are used for evaluation. The ground-based gridded daily precipitation over China with a resolution of 0.25° in China (CN05.1; Wu and Gao, 2013) and the Global Precipitation Climatology Project (GPCP) monthly dataset with a resolution of 2.5° (Adler *et al.*, 2003) are used for rainfall analysis. The CN05.1 is based on the interpolation from over 2,400 observation stations in China. The GPCP is a reanalysis dataset combining satellite-estimated precipitation and surface rain gauge observation. The 1° GPCP data do not span the desired time period, and the 2.5° GPCP data are similar to the 1° data in the focus region (Figure S1, Supporting Information). The fifth-generation climate reanalysis dataset launched

by the European Centre for Medium-Range Weather Forecasts (ERA5; Hersbach *et al.*, 2020) and the Japanese 55-year reanalysis (JRA55; Kobayashi *et al.*, 2015; Harada *et al.*, 2016) are used for the large-scale atmospheric circulation evaluation and moisture budget evaluation.

All the datasets cover the same period as the simulations (from January 1979 to December 2006) and are interpolated to $0.25° \times 0.25°$ resolution using bilinear interpolations.

2.3 | Methods

Monsoon onset, peak, withdrawal, and duration are the four main timings in the EASM procedure. The four timings are defined following the threshold criterion in

Sperber *et al.* (2013), using the pentad as the minimal temporal resolution. The pentad mean records were identified as the 5-day average of the daily values, with pentad one starting on the first of January and no overlap among pentads. We omit February 29th in CN05.1 and ERA5, which have 366 days in the leap years, and calculate the climatic average of each pentad. Monsoon onset is defined as the first pentad in May–September at which the rainfall rate is 5 mm·day^{-1} higher than the January mean rainfall. Monsoon withdrawal is defined as the first pentad after onset when the relative rain falls below 5 mm·day^{-1}. The monsoon peak is the pentad when the maximum relative rainfall rate occurs. Monsoon duration is defined as the pentads from onset to withdrawal.

The Taylor diagram (Taylor, 2001) is used as one of the evaluation methods to evaluate model performances in reproducing the spatial structures of the four primary timings in the EASM. The Taylor diagram provides a visual framework for comparing a suite of variables from model data sets to reference data, including the relative spatial standard deviation ratio (the radial distance), the spatial correlation (the cosine of the azimuthal angle), and the centred root-mean-square error (RMSE, the semicircle with its centre at the reference point "1.0" at the *x*-axis) of model outputs to the reference data. Therefore, a shorter distance to the reference point indicates smaller RMSE and more reasonable reproduction.

3 | RESULTS

3.1 | Precipitation and low-level wind

Precipitation in China is closely related to surface winds and the associated moisture supply from the Pacific and the Indian Ocean. Figure 2a shows the annual mean
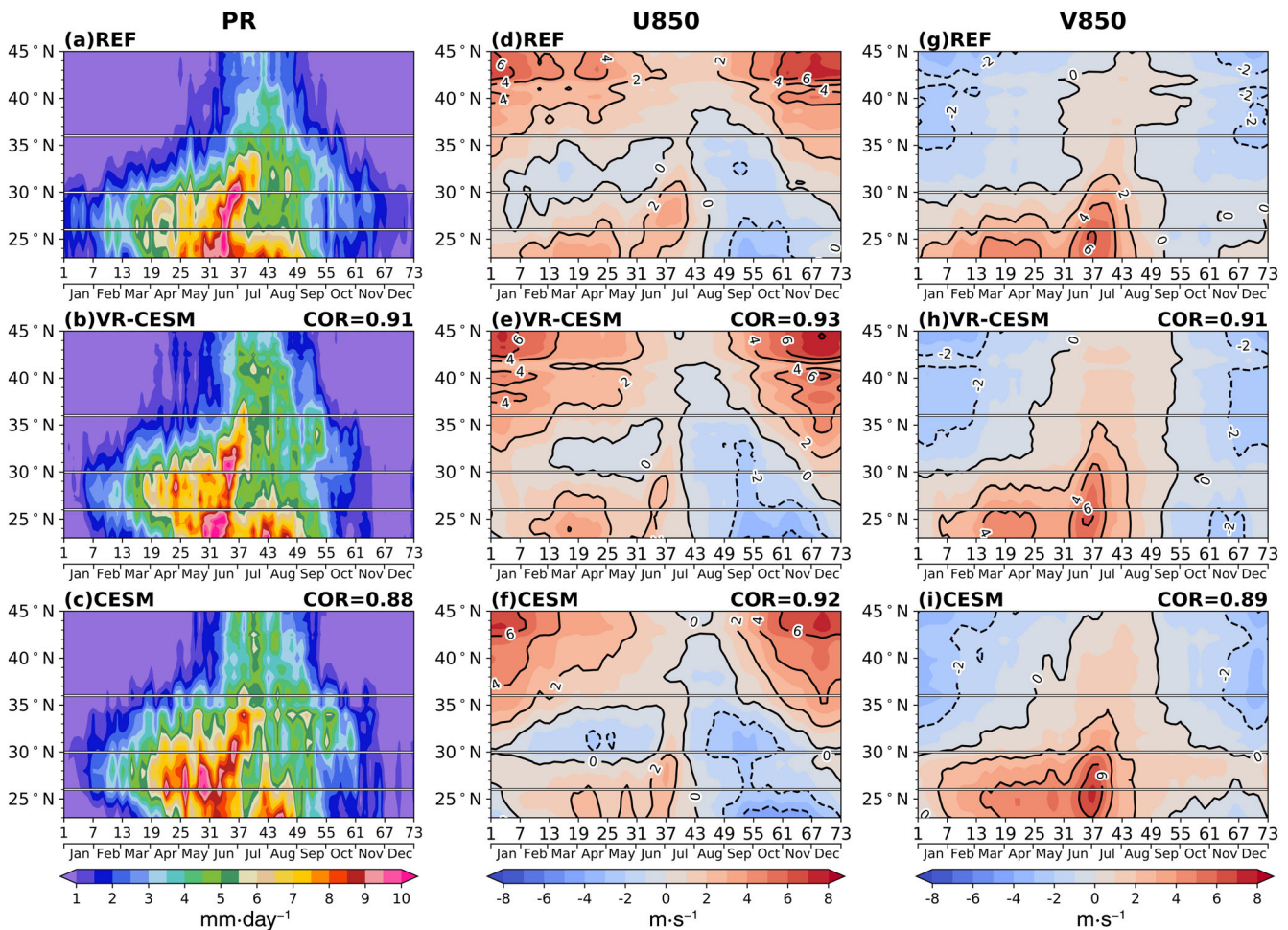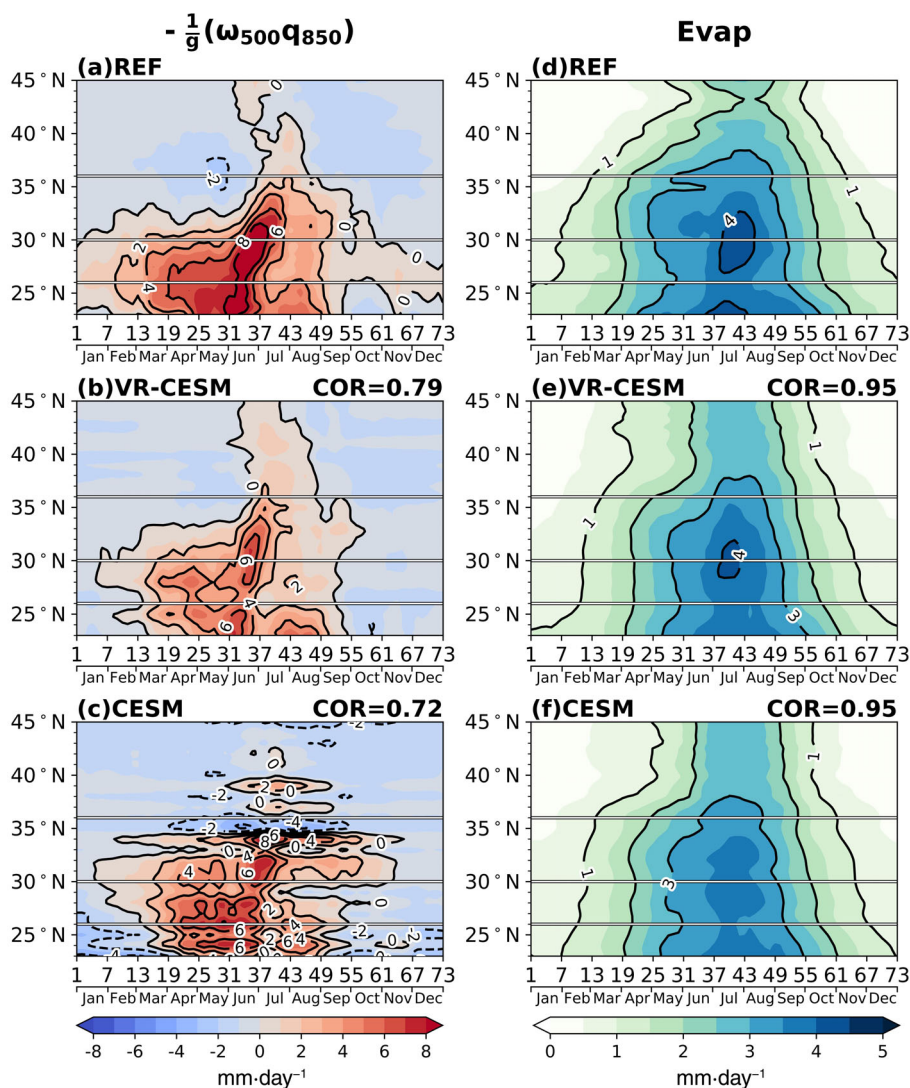

FIGURE 4 (a–c) Latitude–time cross-section of precipitation averaged over the 105°–120°E in reference (CN05.1), VR-CESM and CESM, respectively. Units: mm·day^{-1}. (d–f) and (g–i) The same as (a–c), but for seasonal evolutions of 850 hPa zonal wind (U850) and meridional wind (V850), respectively. Solid grey lines represent the three typical latitudes, 26°N, 30°N, and 36°N. The correlation coefficients between models and the reference data are marked at the top-right corner of corresponding plots [Colour figure can be viewed at wileyonlinelibrary.com]

precipitation in station-based observations CN05.1 and the 850 hPa horizontal wind in ERA5, which serve as the main reference datasets in this study as they have been extensively evaluated. The region of high-precipitation rate located in southeast China is accompanied by the adjacent low-level flow, mainly from the south, which supplies ocean moisture. The GPCP and JRA55 data show high similarities with the reference datasets (Figure 2b) over China with the spatial correlation coefficient of 0.95 for annual mean precipitation. The differences between CN05.1 (ERA5) and GPCP (JRA55) are relatively small (Figure 2e), except for the precipitation differences over the southern border of the TP. The six subregions of China are defined as shown in Figure 1b: four regions east of 105°E (northeast China, north China, Yangtze River valley, south China) and two regions west of 105°E (northwest and southwest China).

VR-CESM reasonably reproduces the spatial distribution of precipitation and atmospheric circulation (Figure 2c) and captures the main precipitation centres well. The VR-CESM biases over eastern China (east of 105°E; Figure 2f), especially over southeast China, are about 0.3 mm·day^{-1}, which is comparable with the differences between CN05.1 and GPCP (Figure 2e), indicating that precipitation and atmospheric circulation are well simulated in VR-CESM. However, VR-CESM generally overestimates precipitation over western China (west of 105°E) and north China. The annual mean precipitation biases in CESM (Figure 2g) are generally larger than in VR-CESM. The largest biases in CESM, both for precipitation and horizontal wind, are evident surrounding the TP. The CESM precipitation is underestimated over the TP but overestimated over the TP's southern and eastern borders. The differences between VR-CESM and CESM (Figure 2h) generally are opposite to the CESM biases (Figure 2g), indicating that VR-CESM results are closer to reference dataset. Significance tests for precipitation errors relative to CN05.1 (the hatched area in Figure 2e–g) demonstrate considerable uncertainty over western China, where

FIGURE 5 Same as Figure 4, but for latitude–time cross-section of (a–c) vertical moisture advection ($-1/g\ w500\ q850$) and (d–f) evapotranspiration averaged over the 105°–120°E. Units: mm·day^{-1}. The vertical moisture advection and evapotranspiration terms are derived from moisture conservation equation as in Jin et al. (2020). The correlation coefficients between models and the reference data are marked at the top-right corner of corresponding plots [Colour figure can be viewed at wileyonlinelibrary.com]

the rainfall amount is relatively small. VR-CESM shows more reasonable performances than CESM over the main rainfall centre east of the TP.

Precipitation over eastern China is greatly affected by the East Asian summer monsoon system. As shown in Figure 3, summer (June–July–August, JJA) precipitation and its biases generally resemble the annual mean results but with larger amplitude. The main summer rain belts are evident over south China and the Yangtze River valley (Figure 3a). Summer rainfall over the Yangtze River valley and in the north contributes to more than 50% of the total annual rainfall. The different spatial structure over south China between annual mean and summer rainfall is due to the contribution of the spring persistent rainfall (Zhang et al., 2013). The spatial correlation between GPCP and CN05.1 is 0.92 with significant differences over the southern part of the TP, where the observations are rare with large uncertainty (Figure 3e). The 850 hPa wind in JRA55 is comparable with the reference (ERA5).

VR-CESM tends to overestimate the summer rainfall over south China, southwest, and north China, but underestimates the rainfall amount along the Yangtze River valley (Figure 3e). The easterly bias over the Yangtze River valley suggests a northward shift of the Northwest Pacific Subtropical High (NWPSH). The northward shift of the NWPSH in the model may contribute to the deficient rainfall along the Yangtze River valley. VR-CESM generally has higher spatial correlation with CN05.1 for summertime precipitation than does CESM. The biases are more pronounced and random in CESM over western China (Figure 3g), where local topography is complex. Given the same physical processes in VR-CESM and CESM, these discrepancies highlight the resolution effects on monsoon rainfall reproduction over regions with complex terrain.

3.2 | The typical seasonal monsoon rainfall evolution

The Asian monsoon system has a significant impact on the climate in eastern China. Figure 4a shows the time–latitude cross-sections of the 5-day average rainfall anomalies over eastern China (105°–120°E). The precipitation over eastern China has four typical monsoon periods: (a) the spring persistent rainfall (SPR) period extends from pentad 12 to 26 over southeast China (Tian and Yasunari, 1998); (b) the south China preflooding season extends from early May to late June; (c) the main summer monsoon period when rainfall gradually spreads northward; (d) and the southward monsoon withdrawal after late August. The south China postflooding season is

also observed from July to September and is mainly related to tropical systems, such as typhoons. VR-CESM can reasonably reproduce the spatial–temporal evolution of EASM precipitation with a correlation coefficient of 0.91 against CN05.1 (Figure 4b), which is higher than that for CESM (0.88). The main rain belts during the whole rainy season are well simulated in VR-CESM but shifted northward in CESM (Figure 4c). The rainfall amount over south of Yangtze River valley (around 30°N) is overestimated in CESM, especially during the SPR from late April to early June. The rainfall amount and duration over north of Yangtze River valley is more reasonably reproduced with less artificial precipitation in VR-CESM than in CESM during the monsoon withdrawal after late August.
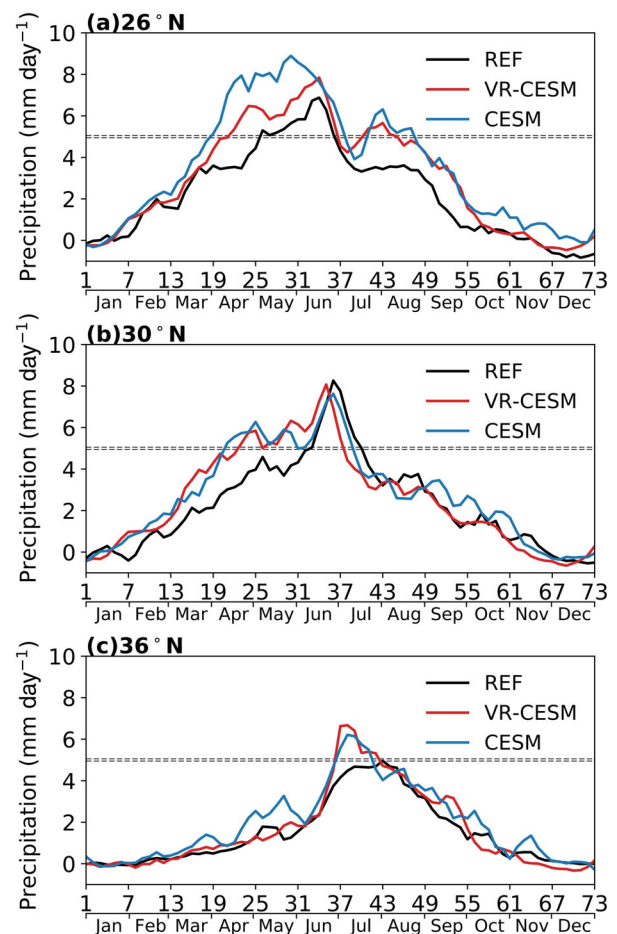
FIGURE 6 The 3-pentad smoothed time series of precipitation anomaly averaged over 105°–120°E along (a) 26°N, (b) 30°N, and averaged over 110°–120°E along (c) 36°N relative to January mean precipitation. The black, red, and blue lines represent the results in Reference (CN05.1), VR-CESM and CESM, respectively. Anomalous precipitation of 5 mm·day^{-1}, that is, the threshold value of monsoon onset and withdrawal, is marked by a dashed grey line [Colour figure can be viewed at wileyonlinelibrary.com]
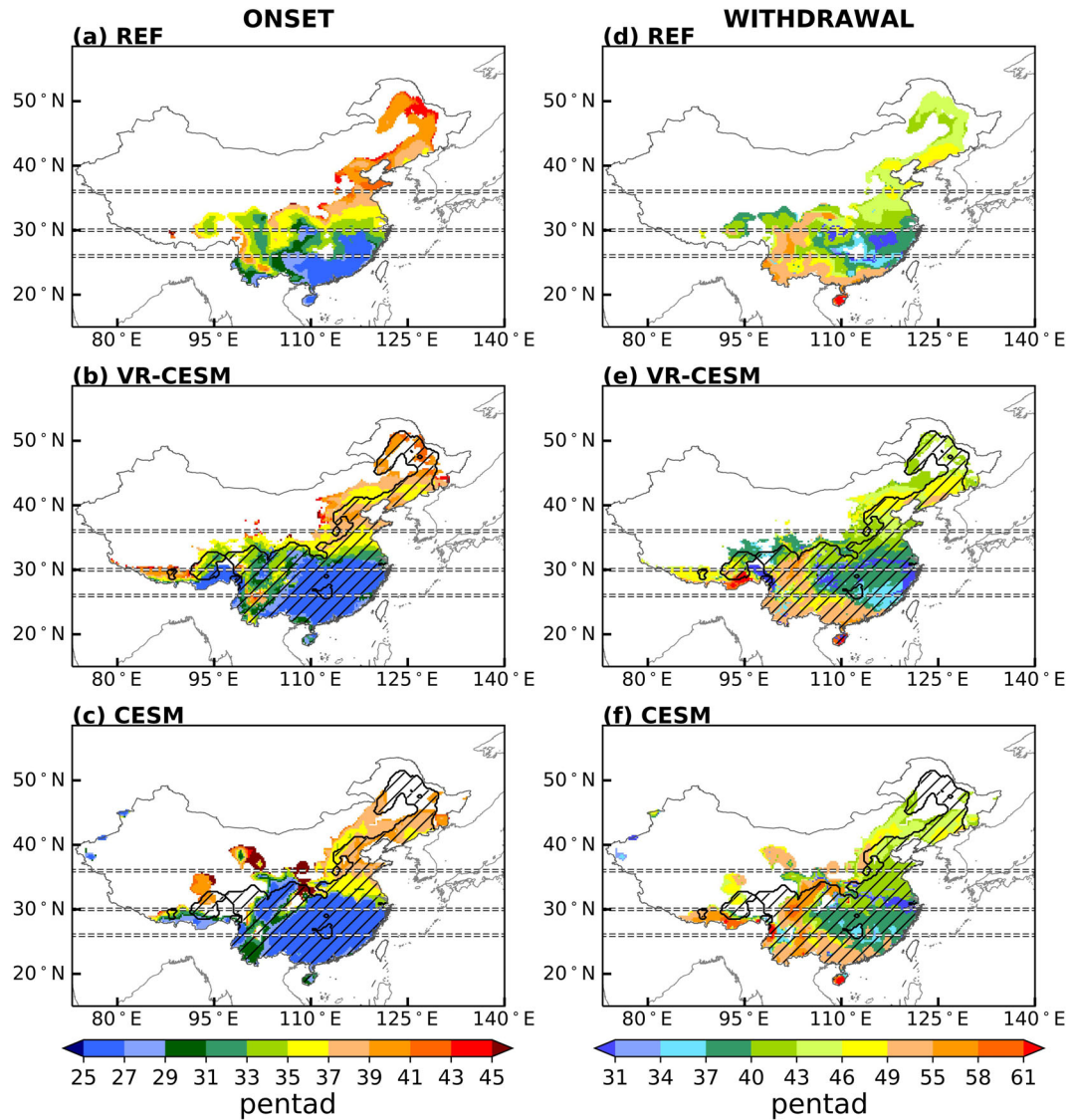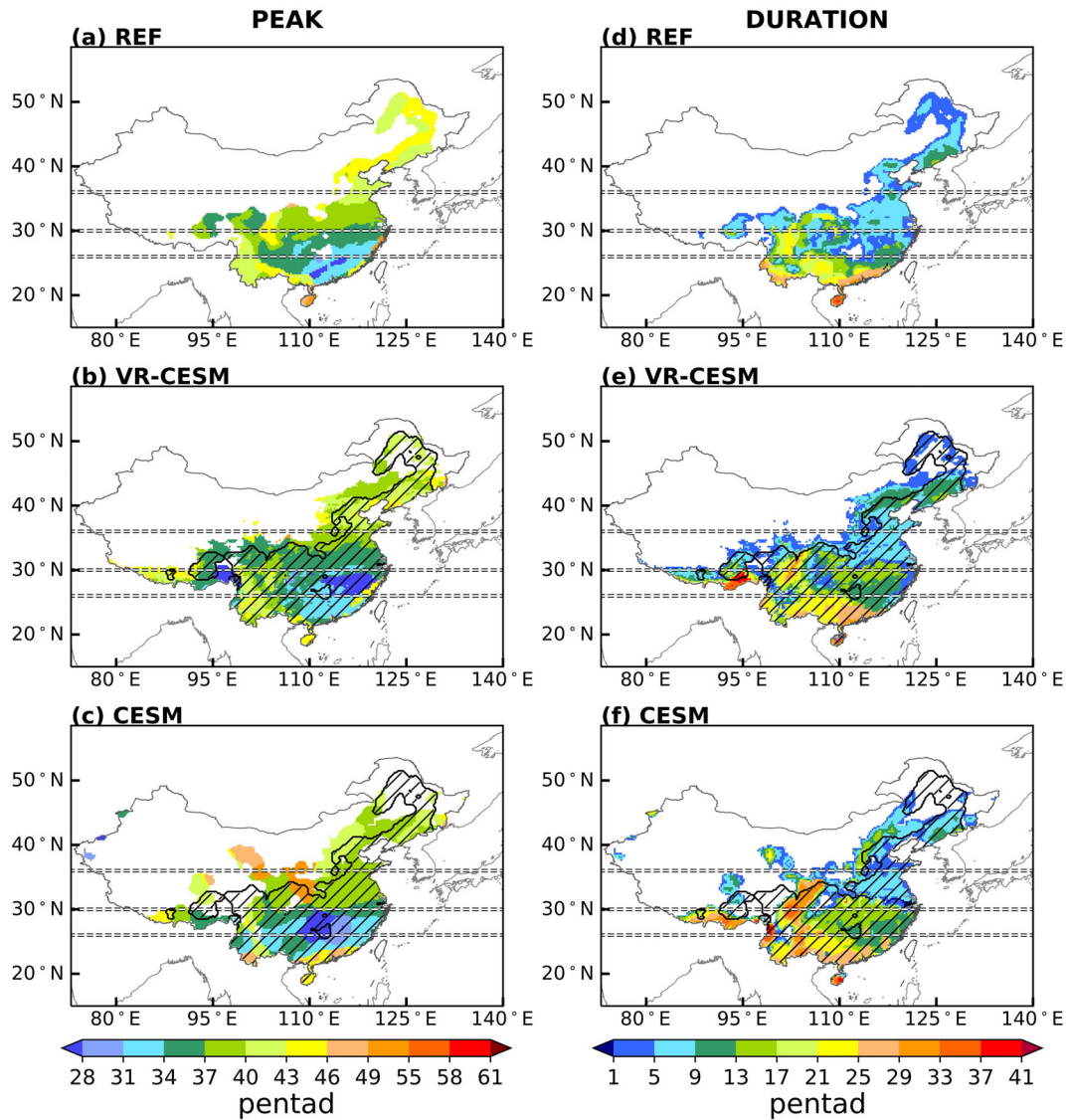
FIGURE 7 (a–c) Monsoon onset pentad and (d–f) monsoon withdrawal pentad in reference (CN05.1) (first row), VR-CESM (second row), and CESM (third row). The hatched lines in the middle and bottom rows represent the monsoon domain in CN05.1. Grey dashed lines mark the three typical latitudes [Colour figure can be viewed at wileyonlinelibrary.com]

The corresponding evolution of the 850 hPa low-level horizontal wind, which supplies monsoon moisture (Ding et al., 2018), is also examined. Developments of both the westerly and southerly flows resemble the monsoon rainfall propagations (Figure 4d,g). The westerly moisture supply is a crucial source of water for precipitation over south China, especially during the SPR period (Zhang et al., 2009). The southerly flow contributes to water supply during the monsoon season and is the main driver for the northward movement of the monsoon rainbelt. VR-CESM captures the spatial distribution of westerly flow well (Figure 4e). The evolution and intensity of the southerly flow are also well reproduced in VR-CESM (Figure 4h). In CESM, the primary westerly moisture source during the SPR period is less organized

(Figure 4f), leading to some intermittent rainy periods over south China. The southerly flow in CESM is overestimated, which is responsible for the excessive SPR and northward shifted rainbelt. The southerly–northerly flow transition south of 30°N in early September (around pentad 50) is missing in CESM (Figure 4i), which is responsible for the abnormally overestimated autumn rainfall north of the Yangtze River valley (Figure 4c).

Based on principles of moisture conservation (Jin et al., 2020), the vertical moisture advection plays a key role in the EASM evolution. We focus on the time–latitude cross-sections of the vertical moisture component and the evapotranspiration over eastern China (105°–120°E; Figure 5) as the horizontal component is relatively small and can be neglected. As presented by Jin et al.

FIGURE 8 Same as Figure 7, but for (a–c) monsoon peak pentad and (d–f) monsoon duration [Colour figure can be viewed at wileyonlinelibrary.com]

(2020), the vertical moisture advection can be approximated as $-\frac{1}{g}\omega_{500}q_{850}$, where g is the gravitational acceleration, ω_{500} is the vertical velocity at 500 hPa, and q_{850} is the specific humidity at 850 hPa. The vertical moisture advection of VR-CESM (Figure 5b) shows better similarity and more comparable amplitude with the reference (Figure 5a) than CESM (Figure 5c); the correlation coefficients are about 0.79 and 0.72, respectively. The overestimated vertical moisture advection in CESM is largely responsible for the excessive precipitation during the postflooding season over south China (around pentad 43) and also during the southward monsoon withdrawal period after late August over the Yangtze River valley. The contribution of evapotranspiration is generally more pronounced during summertime and does not show as much of a northward shift over time (Figure 5d–f). Both

VR-CESM and CESM show high performances in reproducing the evapotranspiration with correlation coefficients of 0.95. As VR-CESM better captures the vertical moisture advection than does CESM, VR-CESM also reproduces the EASM evolution better than CESM.

Previous studies have shown that the main summer monsoon period is characterized by two abrupt northward jumps and three stationary periods (Ding and Chan, 2005) over south China (around 26°N), the Yangtze River valley (around 30°N), and north China (around 36°N), respectively. Figure 6 further examines the evolution of rainfall anomalies relative to January mean precipitation for each dataset at these three typical latitudes (marked by grey lines in Figure 4) over eastern China. The first pentad when the anomalies exceed 5 mm·day^{-1} is defined as the monsoon onset date. At 26°N, the
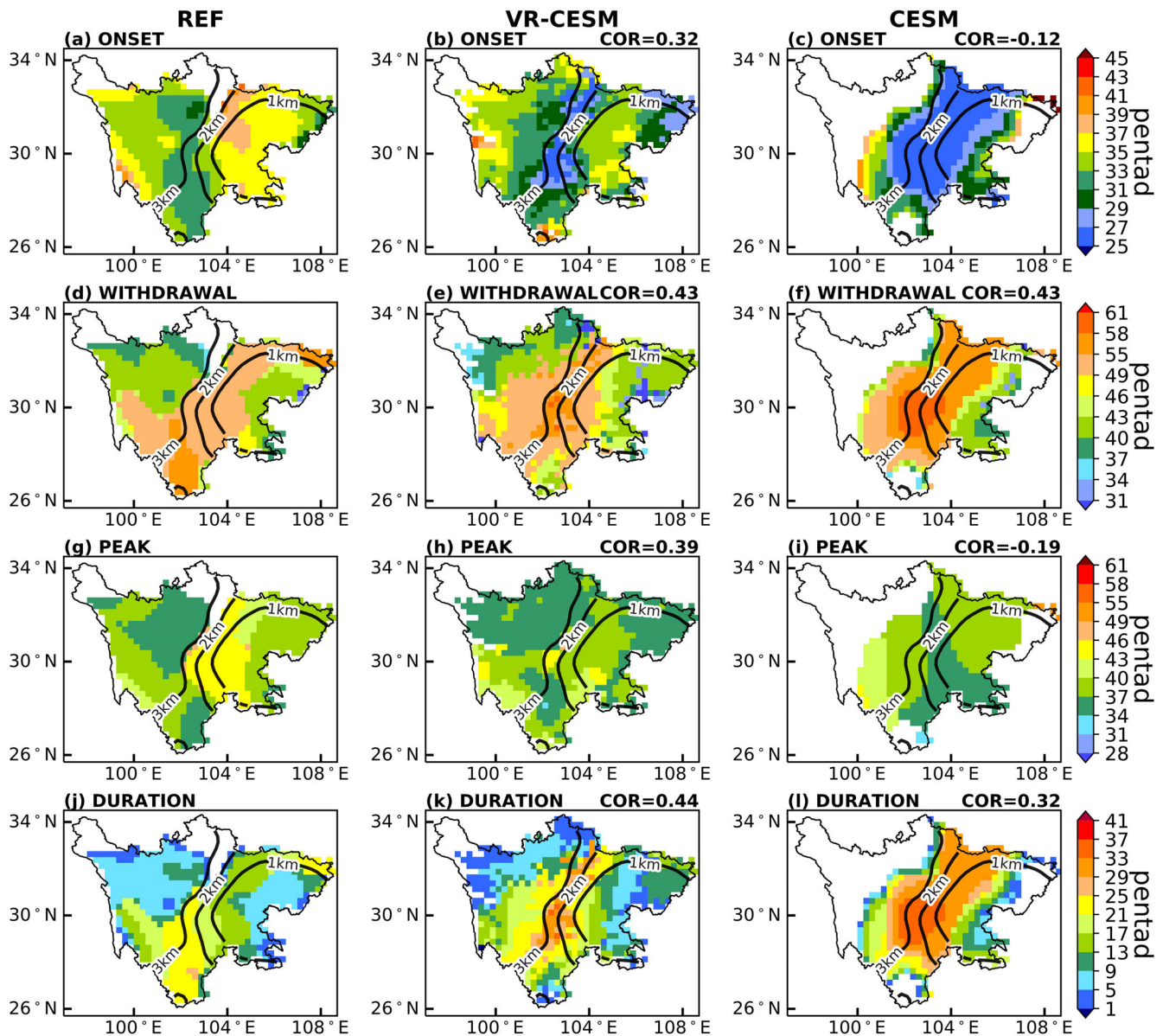
FIGURE 9 Monsoon procedures zoomed over Sichuan Province, China. (a–c) Monsoon onset pentad, (d–f) monsoon withdrawal pentad, (g–i) monsoon peak pentad, and (j–l) monsoon duration in reference (CN05.1) (left column), VR-CESM (middle column), and CESM (right column). Black contours represent regional terrain height (unit: km). The correlation coefficients between models and the reference data are marked at the top-right corner of corresponding plots [Colour figure can be viewed at wileyonlinelibrary.com]

preflooding season lasts from early May to late June and peaks in mid-June (Figure 6a). Rainfall in the following postflooding period is relatively weaker and below the monsoon threshold. The earlier monsoon onset and the overestimated preflooding and postflooding precipitation over south China are problems in both models, but more pronounced in CESM. The earlier monsoon onset is also evident at 30°N, but model precipitation magnitudes are much better starting in June. At 36°N, the rainy season is relatively short, peaking in early August (Figure 6c). Both VR-CESM and CESM overestimate the monsoon duration over the three typical latitudes.

Generally, VR-CESM shows better performances than CESMs in reproducing the seasonal variability of the East Asian monsoon rainfall over China, which is closely related to improvements in simulating the low-level horizontal wind and the vertical moisture advection.

3.3 | The four main timings of East Asian monsoon

Based on the monsoon threshold criteria introduced in section 2, the spatial features of the four main timings of
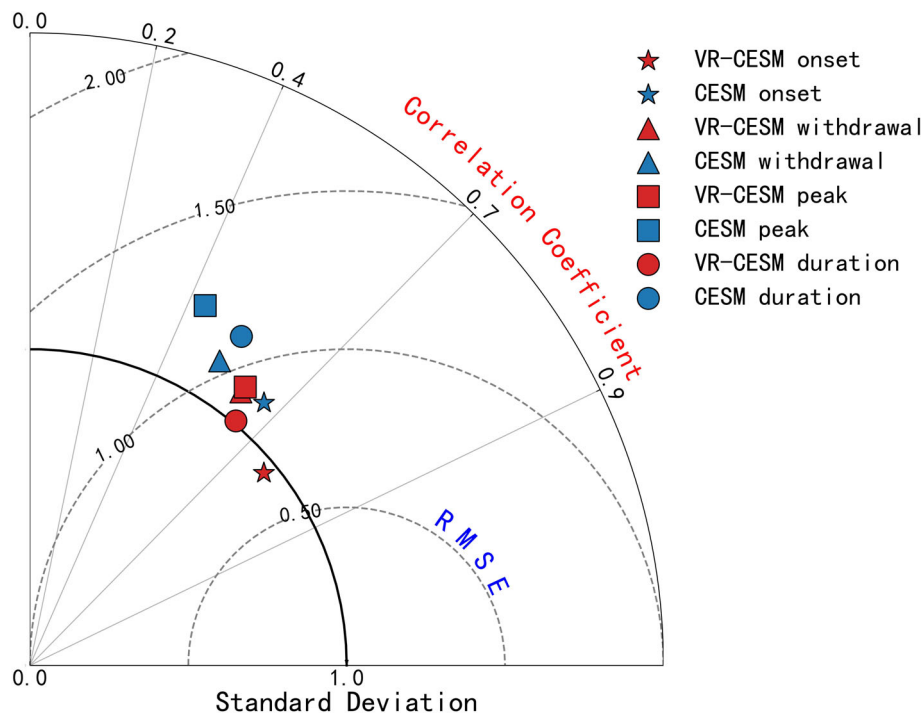
FIGURE 10 Taylor diagram for the spatial distributions of monsoon onset, withdrawal, peak, and duration in Figures 7 and 8. The radial coordinate shows the standard deviation of the spatial pattern normalized by the standard deviation of reference data. The azimuthal variable shows the correlation of the modelled spatial pattern with the spatial pattern in reference data. The reference data is CN05.1 over the monsoon domain [Colour figure can be viewed at wileyonlinelibrary.com]

the East Asian monsoon are examined in Figures 7 and 8, including monsoon onset, withdrawal, peak, and duration. The reference datasets show that the East Asian monsoon system significantly impacts on the southern and eastern parts of China. The spatial–temporal evolution of the monsoon is fairly well represented by VR-CESM as compared to CESM, even though both models generally estimate earlier onset.

Monsoon onset in the reference (Figure 7a) first establishes in south China at around the 25th pentad (early May), then gradually advances to the North, and reaches northeast China at around the 39th pentad (mid-July). The blank region over the Hunan province is due to relatively complex local topography, where the anomalies relative to January mean precipitation are lower than 5 mm·day^{-1}. In the Yangtze River valley both models simulate onset about 4.5 pentads earlier than the reference data. Over Sichuan Province, the eastern boundary of the TP, the monsoon has early establishment over the high topographic regions in the west and later establishment over the Sichuan Basin in the east (Figure 9a). The northward migration of monsoon onset and the typical features over the Sichuan Province with complex terrain are both well captured by VR-CESM (Figures 7b and 9b) but are not reproduced by CESM (Figures 7c and 9c). Major discrepancies in CESM exist at the edges of the monsoon area, such as over the southeast boundary of the TP and the southern and eastern parts of Inner Mongolia. The monsoon impact area west of 105°E where the elevation exceeds 3 km is underestimated in CESM

(Figure 9c) but well reproduced in VR-CESM. The advantage of VR-CESM over complex terrain is also evident in the simulation of monsoon withdrawal, peak, and duration (Figures 7e and 8b,e).

The monsoon starts to retreat from northeast China at around the 43rd to 46th pentad (early August; Figure 7d) and then withdraws southward quickly to the southwest and south China at around the 49th to 55th pentad. The latest withdrawal over the southwest China occurs over eastern Sichuan Province with steep topography. VR-CESM (Figure 7e) can generally reproduce the southward monsoon withdrawal and the late withdrawal near the TP. However, CESM fails to accurately simulate monsoon withdrawal over the northern and western edge monsoon domains (Figure 7f).

The evolution of the monsoon peak follows that of the monsoon onset. In the reference dataset (Figure 8a), the monsoon peak establishes firstly in the south at around the 31st pentad (early June), gradually moving north and arriving in northeast China at around the 43rd pentad (late July), which is associated with the flooding season in northeast China. In VR-CESM (Figure 8b), the monsoon peaks earlier than the reference over the Yangtze River valley, consistent with the earlier onset. The best matches for the monsoon peak are located over southwest and northeast China. The biases are generally larger in CESM over the entire monsoon domain.

Monsoon duration is generally longer over south China and southwest China (longer than 13 pentads) than over the Yangtze River valley and north China (Figure 8d).

Similar to the other metrics, the monsoon duration patterns are more reasonable in VR-CESM than in CESM (Figure 8e,f), with the duration over the Yangtze River valley about 1.6 pentads longer in VR-CESM and about 4 pentads longer in CESM than in the reference data.

For quantitative comparison, the spatial distributions of the four primary timings of EASM are further analysed by Taylor diagrams. As shown in Figure 10, the spatial standard deviations of all the four primary monsoon timings are reasonably captured by both models with the relative spatial standard deviation ratio close to 1.0. The monsoon onset is generally the best-simulated feature among the four timings, and the monsoon peak is the most challenging feature. VR-CESM has higher spatial correlations with the reference data than CESM does and thus better captures the spatial patterns of all the timings. The spatial correlation coefficients of all four timings in VR-CESM are about 0.1 higher than those in CESM, mainly due to the improvement over northeast and southwest China, which represent the northern frontier of the EASM and the region with the most complex topography, respectively. Therefore, refined resolution is essential for robust reproduction of the EASM, especially over the edges of the monsoon domain and regions with complex topography.

3.4 | Land–sea thermal contrast

The thermal contrast between the East Asian continent and the oceans drives the monsoon circulation and is essential to the establishment, seasonal evolution, and variations of the EASM in China (e.g., Wu *et al.*, 2007; Dai *et al.*, 2013; Liu *et al.*, 2020). The VR-CESM and CESM simulations are both AMIP-type runs, where the sea surface temperature is prescribed by observation-based reanalysis data (HadISST). Therefore, the biases in land–sea thermal contrast should be driven by air temperature biases over land.

With respect to temperature, the TP may play a vital role even though it is not on the coast. As shown in Figure 11, the warm bias of summertime T500 is pronounced over the highest and most complex topographical region, the TP (75°–105°E, 25°–40°N). The TP is a large heat source in summer because the air column over the TP descends in winter and ascends in summer, working as an air pump to transfer heat to the upper atmosphere (Wu *et al.*, 2007). The warm air over the TP enhances the summer land-sea thermal contrasts between the East Asia continent and the West Pacific Ocean and greatly impacts the onset of EASM. The T500 shows a warm bias of 1°C over the TP in VR-CESM (Figure 11b), and about a 2°C warm bias with many
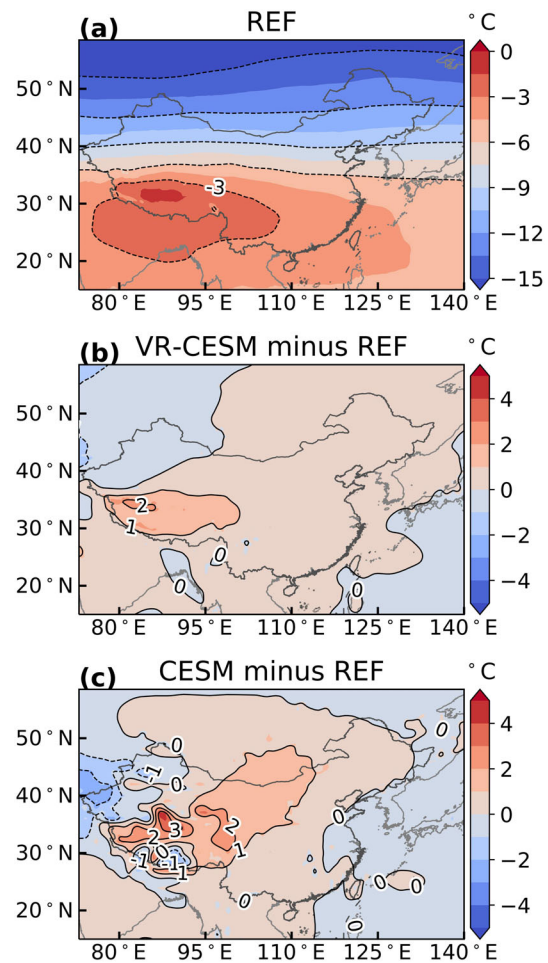

FIGURE 11 Summertime (JJA) air temperature at 500 hPa (T500) in (a) reference (ERA5), and the biases in (b) VR-CESM and (c) CESM. Units: °C [Colour figure can be viewed at wileyonlinelibrary.com]
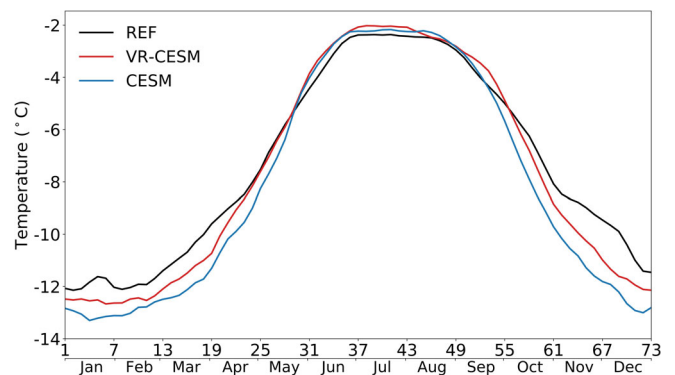
FIGURE 12 Evolutions of the regional mean air temperature at 500 hPa over the Tibetan Plateau (20°–30°N, 75°–105°E). Units: °C [Colour figure can be viewed at wileyonlinelibrary.com]

singular points of negative bias in CESM (Figure 11c). Evolutions of T500 over the TP show that model biases are even larger during the premonsoon and postmonsoon
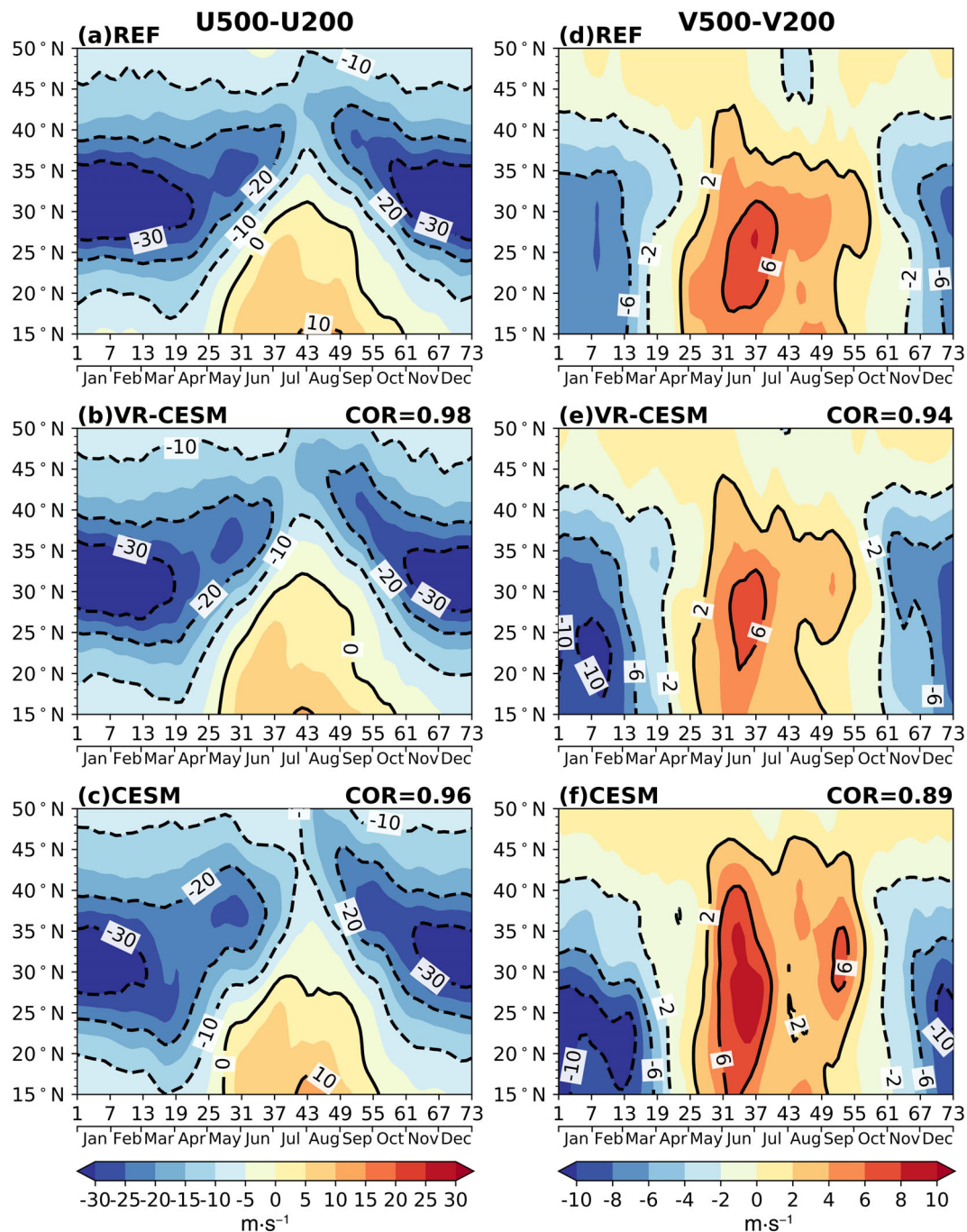
FIGURE 13 (a–c) Latitude–time cross-section of the differences between U200 and U500 averaged over the 105°–120°E. Units: m·s⁻¹. (d–f) Same as (a–c), but for the differences between V200 and V500. The correlation coefficients between models and the reference data are marked at the top-right corner of corresponding plots [Colour figure can be viewed at wileyonlinelibrary.com]

periods (Figure 12). The colder biases in CESM than in VR-CESM indicate stronger meridional (north–south) and zonal (west–east) temperature gradients, which trigger earlier monsoon onset and withdrawal in CESM.

Considering the contribution of latent heating and the expanding warm air over land, the land–sea thermal contrast in the mid-upper troposphere may play a more important role in EASM evolution than the contrast in

the lower troposphere (Dai et al., 2013). Furthermore, Qi et al. (2008) found that the seasonal transition of zonal thermal contrast is closely related to subtropical monsoon onset in East Asia. The effect of land–sea thermal contrast on monsoon circulation can be estimated by the thermal wind equations (Holton, 2004). Following Dai et al. (2013), the thermal contrasts in the north–south and west–east directions are defined as U500 minus U200

FIGURE 14 The evolution of standardized East Asian summer monsoon index (EASMI) in ERA5 (black line), VR-CESM (red line), and CESM (blue line). The definition of EASMI follows Wang and Fan (1999) [Colour figure can be viewed at wileyonlinelibrary.com]
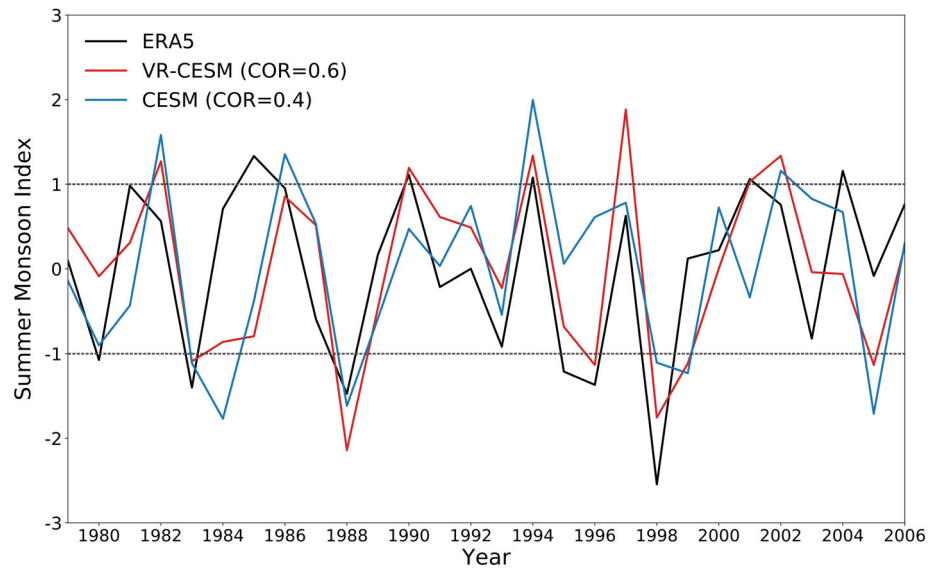
and V500 minus V200, respectively. As shown in Figure 13a,d, both the north–south and west–east gradients are intensified with the growth of T500 over the TP (Figure 12) during the monsoon period. In the south, the temperature gradient transitions around pentad 25th in spring, when the land–sea thermal contrast turns from "warm-ocean/cold-continent" to "cold-ocean/warm-continent." This also corresponds well with monsoon onset. The temperature gradient reverses again around pentad 55, corresponding with the end of the monsoon season. The evolution of the meridional temperature gradient is generally well reproduced by both models. The correlation coefficient with the reference data is 0.98 for VR-CESM and 0.96 for CESM. VR-CESM simulates the west–east temperature gradient during the monsoon period more reasonably than CESM (Figure 13e,f), which clearly overestimates this contrast. This larger thermal contrast in CESM is largely responsible for the intensified water supply from the south (Figure 4i) and for the earlier monsoon onset and the abundant precipitation over the Yangtze River valley during the monsoon withdrawal period.

The more reasonably reproduced air temperature over the TP and the related improvements in zonal temperature gradient are important factors in VR-CESM's improved seasonal evolution of the EASM and even the interannual variability of EASM as compared to CESM. Lower troposphere winds can characterize the strength of the EASM as it relates to land–sea thermal contrast. The EASM index in Wang and Fan (1999) (WF index) is defined as the U850 in 5°–15°N, 90°–130°E minus U850 in 22.5°–32.5°N, 110°–140°E. This definition reflects variations in both the western North Pacific monsoon trough and the subtropical high. As shown in Figure 14, VR-CESM better captures the evolution and the strength of EASM index than does CESM, such as the high EASM

indices in 1990, 1994, 2001, and low EASM indices in 1996 and 1998. The EASM index correlation with ERA5 is also higher in VR-CESM (0.6) than in CESM (0.4). Since the TP is such a large, dramatic topographical feature, these improvements are at least in part related to the refined resolution in VR-CESM.

4 | CONCLUSION

In this study, we evaluate the performance of VR-CESM with regionally refined resolution over eastern China of 14 km in simulating the East Asian summer monsoon. The VR-CESM results are compared with the corresponding coarse-resolution (quasi-uniform 1°) model CESM to investigate the benefits of refining horizontal resolution. The main findings are as follows:

1. The spatial distribution of precipitation and circulation over China are well reproduced by VR-CESM, especially over eastern China. The precipitation and wind biases in CESM are larger than those in VR-CESM, particularly surrounding the Tibetan Plateau.
2. The rainy season extends from early May to September over East Asia, featuring a meridional seasonal evolution. The typical features are attributed to the evolution of southerly flow and vertical moisture advection. Generally, the seasonal evolution of precipitation is better simulated in VR-CESM than in CESM, including the well-organized SPR, the precipitation during monsoon withdrawal period over north China, and the postflooding over south China.
3. The four critical timings of the East Asian monsoon (monsoon onset, withdrawal, peak, and duration) are well captured by VR-CESM. The spatial correlation

coefficients of the four critical timings in VR-CESM with respect to reference data are about 0.1 higher than those in CESM. Specifically, CESM shows significant deficiencies at the western edge of the monsoon area of the reference data, as defined by the monsoon threshold criteria in Sperber *et al.* (2013), where the topography is complex. Furthermore, the models are most successful at simulating monsoon onset and least successful at simulating the peak.

4. The evolution of air temperature over the TP, which is closely related to zonal thermal contrast, is important for the evolution of East Asian monsoon. The better simulated air temperature over the TP in VR-CESM improves thermal contrast and EASM evolution simulation over CESM and is likely due to the refined resolution over regions with complex topography.

Overall, East Asian summer monsoon evolution in VR-CESM with refined resolution over eastern China is better than that in the quasi-uniform 1° resolution model CESM, indicating that model performances, especially over the TP and northern edge of EASM, are sensitive to regional resolution.

ACKNOWLEDGEMENTS

ORCID

Haonan Zhu https://orcid.org/0000-0002-7703-5565
Jie Zhang https://orcid.org/0000-0002-8925-1011
Xiaoge Xin https://orcid.org/0000-0001-9712-5368

REFERENCES

Adler, R.F., Huffman, G.J., Chang, A., Ferraro, R., Xie, P.P., Janowiak, J., Rudolf, B., Schneider, U., Curtis, S., Bolvin, D., Gruber, A., Susskind, J., Arkin, P. and Nelkin, E. (2003) The version-2 global precipitation climatology project (GPCP) monthly precipitation analysis (1979–present). *Journal of Hydrometeorology*, 4(6), 1147–1167. https://doi.org/10.1175/1525-7541(2003)004<1147:TVGPCP>2.0.CO;2.

Cha, D.H., Jin, C.S., Moon, J.H. and Lee, D.K. (2016) Improvement of regional climate simulation of East Asian summer monsoon by coupled air–sea interaction and large-scale nudging. *International Journal of Climatology*, 36(1), 334–345. https://doi.org/10.1002/joc.4349.

Chen, C.A., Hsu, H.H. and Liang, H.C. (2021) Evaluation and comparison of CMIP6 and CMIP5 model performance in simulating the seasonal extreme precipitation in the Western North Pacific and East Asia. *Weather and Climate Extremes*, 31, 100303. https://doi.org/10.1016/j.wace.2021.100303.

Chen, F.H., Xu, Q.H., Chen, J.H., Birks, H.J.B., Liu, J.B., Zhang, S.R., Jin, L.Y., An, C.B., Telford, R.J.T., Cao, X.Y., Wang, Z.L., Zhang, X.J., Selvaraj, K., Lu, H.Y., Li, Y.C., Zheng, Z., Wang, H.P., Zhou, A.F., Dong, G.H., Zhang, J.W., Huang, X.Z., Bloemendal, J., and Rao, Z.G. (2015) East Asian summer monsoon precipitation variability since the last deglaciation. *Scientific Reports*, 5(1), 1–11. https://doi.org/10.1038/srep11186.

Chen, J. and Bordoni, S. (2014) Orographic effects of the Tibetan Plateau on the East Asian summer monsoon: an energetic perspective. *Journal of Climate*, 27(8), 3052–3072. https://doi.org/10.1175/jcli-d-13-00479.1.

Dai, A.G., Li, H.M., Sun, Y., Hong, L.C., Ho, L., Chou, C., and Zhou, T.J. (2013) The relative roles of upper and lower tropospheric thermal contrasts and tropical influences in driving Asian summer monsoons. *Journal of Geophysical Research: Atmospheres*, 118, 7024–7045. https://doi.org/10.1002/jgrd.50565.

Ding, Y.H. and Chan, J.C.L. (2005) The East Asian summer monsoon: an overview. *Meteorology and Atmospheric Physics*, 89(1–4), 117–142. https://doi.org/10.1007/s00703-005-0125-z.

Ding, Y.H., Si, D., Liu, Y.J., Wang, Z.Y., Li, Y., Zhao, L. and Song, Y.F. (2018) On the characteristics, driving forces and inter-decadal variability of the East Asian summer monsoon. *Chinese Journal of Atmospheric Sciences*, 42, 533–558 (in Chinese). https://doi.org/10.3878/j.issn.1006-9895.1712.17261.

Gates, W.L. (1992) AMIP: the Atmospheric Model Intercomparison Project. *Bulletin of the American Meteorological Society*, 73(12), 1962–1970. https://doi.org/10.1175/1520-0477(1992)073<1962:atamip>2.0.co;2.

Gettelman, A., Callaghan, P., Larson, V.E., Zarzycki, C.M., Bacmeister, J.T., Lauritzen, P.H., Bogenschutz, P.A. and Neale, R.B. (2018) Regional climate simulations with the community earth system model. *Journal of Advances in Modeling Earth Systems*, 10(6), 1245–1265. https://doi.org/10.1002/2017ms001227.

Gettelman, A., Morrison, H., Santos, S. and Bogenschutz, P. (2015) Advanced two-moment bulk microphysics for global models. Part II: global model solutions and aerosol–cloud interactions. *Journal of Climate*, 28(3), 1288–1307. https://doi.org/10.1175/jcli-d-14-00103.1.

Gibelin, A.L. and Déqué, M. (2003) Anthropogenic climate change over the Mediterranean region simulated by a global variable resolution model. *Climate Dynamics*, 20(4), 327–339. https://doi.org/10.1007/s00382-002-0277-1.

Harada, Y., Kamahori, H., Kobayashi, C., Endo, H., Kobayashi, S., Ota, Y., Onoda, H., Onogi, K., Miyaoka, K. and Takahashi, K. (2016) The JRA-55 reanalysis: representation of atmospheric circulation and climate variability. *Journal of the Meteorological Society of Japan*, 94(3), 269–302. https://doi.org/10.2151/jmsj.2016-015.

Hersbach, H., Bell, B., Berrisford, P., Hirahara, S., Horányi, A., Muñoz-Sabater, J., Nicolas, J., Peubey, C., Radu, R., Schepers, D., Simmons, A., Soci, C., Abdalla, S., Abellan, X., Balsamo, G., Bechtold, P., Biavati, G., Bidlot, J., Bonavita, M., Chiara, G., Dahlgren, P., Dee, D., Diamantakis, M.,

Dragani, R., Flemming, J., Forbes, R., Fuentes, M., Geer, A., Haimberger, L., Healy, S., Hogan, R.J., Hólm, E., Janisková, M., Keeley, S., Laloyaux, P., Lopez, P., Lupu, C., Radnoti, G., Rosnay, P., Rozum, I., Vamborg, F., Villaume, S. and Thépaut, J.N. (2020) The ERA5 global reanalysis. *Quarterly Journal of the Royal Meteorological Society*, 146, 1999–2049. https://doi.org/10.1002/qj.3803.

Holton, J.R. (2004) In: Dmowska, R., Holton, J.R. and Rossby, H.T. (Eds.) *An Introduction to Dynamic Meteorology. International Geophysics Series*, Vol. 88, 4th edition. Burlington, MA: Elsevier, 535 pp.

Huang, D., Yan, P., Zhu, J., Zhang, Y., Kuang, X. and Cheng, J. (2018) Uncertainty of global summer precipitation in the CMIP5 models: a comparison between high-resolution and low-resolution models. *Theoretical and Applied Climatology*, 132(1), 55–69. https://doi.org/10.1007/s00704-017-2078-9.

Jin, C., Wang, B. and Liu, J. (2020) Future changes and controlling factors of the eight regional monsoons projected by CMIP6 models. *Journal of Climate*, 33(21), 9307–9326. https://doi.org/10.1175/JCLI-D-20-0236.1.

Kitoh, A. and Kusunoki, S. (2008) East Asian summer monsoon simulation by a 20-km mesh AGCM. *Climate Dynamics*, 31(4), 389–401. https://doi.org/10.1007/s00382-007-0285-2.

Kobayashi, S., OTA, Y. and Harada, Y. (2015) The JRA-55 reanalysis: general specifications and basic characteristics. *Journal of the Meteorological Society of Japan*, 93(1), 5–48. https://doi.org/10.2151/jmsj.2015-001.

Liu, Y.M., Lu, M.M., Yang, H.J., Duan, A., He, B., Yang, S. and Wu, G.X. (2020) Land–atmosphere–ocean coupling associated with the Tibetan Plateau and its climate impacts. *National Science Review*, 7, 534–552. https://doi.org/10.1093/nsr/nwaa011.

Ogata, T., Johnson, S.J., Schiemann, R., Demory, M.E., Mizuta, R., Yoshida, K. and Osamu, A. (2017) The resolution sensitivity of the Asian summer monsoon and its inter-model comparison between MRI-AGCM and MetUM. *Climate Dynamics*, 49(9), 3345–3361. https://doi.org/10.1007/s00382-016-3517-5.

Park, S. and Bretherton, C.S. (2009) The University of Washington shallow convection and moist turbulence schemes and their impact on climate simulations with the community atmosphere model. *Journal of Climate*, 22(12), 3449–3469. https://doi.org/10.1175/2008jcli2557.1.

Qi, L., He, J.H., Zhang, Z.Q. and Song, J.N. (2008) Seasonal cycle of the zonal land–sea thermal contrast and East Asian subtropical monsoon circulation. *Chinese Science Bulletin*, 53(1), 131–136. https://doi.org/10.1007/s11434-007-0518-0.

Rahimi, S.R., Wu, C.L., Liu, X.H. and Brown, H. (2019) Exploring a variable-resolution approach for simulating regional climate over the Tibetan Plateau using VR-CESM. *Journal of Geophysical Research: Atmospheres*, 124, 4490–4513. https://doi.org/10.1029/2018JD028925.

Rhoades, A.M., Huang, X.Y., Ullrich, P.A. and Zarzycki, C.M. (2016) Characterizing Sierra Nevada snowpack using variable-resolution CESM. *Journal of Applied Meteorology and Climatology*, 55(1), 173–196. https://doi.org/10.1175/jamc-d-15-0156.1.

Ringler, T.D., Jacobsen, D., Gunzburger, M., Ju, L., Duda, M. and Skamarock, W. (2011) Exploring a multiresolution modeling approach within the shallow-water equations. *Monthly Weather Review*, 139(11), 3348–3368. https://doi.org/10.1175/mwr-d-10-05049.1.

Sperber, K.R., Annamalai, H., Kang, I.S., Kitoh, A., Moise, A., Turner, A., Wang, B. and Zhou, T. (2013) The Asian summer monsoon: an intercomparison of CMIP5 vs. CMIP3 simulations of the late 20th century. *Climate Dynamics*, 41(9–10), 2711–2744. https://doi.org/10.1007/s00382-012-1607-6.

Syed, F.S., Iqbal, W., Syed, A.A.B. and Rasul, G. (2014) Uncertainties in the regional climate models simulations of South Asian summer monsoon and climate change. *Climate Dynamics*, 42(7–8), 2079–2097. https://doi.org/10.1007/s00382-013-1963-x.

Taylor, K.E. (2001) Summarizing multiple aspects of model performance in a single diagram. *Journal of Geophysical Research: Atmospheres*, 106(D7), 7183–7192. https://doi.org/10.1029/2000jd900719.

Tian, S.F. and Yasunari, T. (1998) Climatological aspects and mechanism of spring persistent rains over central China. *Journal of the Meteorological Society of Japan*, 76(1), 57–71. https://doi.org/10.2151/jmsj1965.76.1_57.

Ullrich, P. (2014) Squadgen: spherical quadrilateral grid generator, University of California, Davis, Climate and Global Change Group software. Available at: http://climate.ucdavis.edu/squadgen.php.

Wang, B. and Fan, Z. (1999) Choice of South Asian summer monsoon indices. *Bulleting of the American Meteorological Society*, 80(4), 629–638. https://doi.org/10.1175/1520-0477(1999)080<0629:COSASM>2.0.CO;2.

Wang, M.N. and Ullrich, P. (2018) Marine air penetration in California's Central Valley: meteorological drivers and the impact of climate change. *Journal of Applied Meteorology and Climatology*, 57(1), 137–154. https://doi.org/10.1175/jamc-d-17-0089.1.

Wang, M.N., Ullrich, P. and Millstein, D. (2018) The future of wind energy in California: future projections with the variable-resolution CESM. *Renewable Energy*, 127, 242–257. https://doi.org/10.1016/j.renene.2018.04.031.

Wu, C.L., Liu, X.H., Lin, Z.H., Rhoades, A.M., Ullrich, P.A., Zarzycki, C.M., Lu, Z. and Rahimi-Esfarjani, S.R. (2017) Exploring a variable-resolution approach for simulating regional climate in the Rocky Mountain region using the VR-CESM. *Journal of Geophysical Research: Atmospheres*, 122(20), 10939–10965. https://doi.org/10.1002/2017jd027008.

Wu, G.X., Liu, Y.M., Wang, T.M., Wan, R.J., Liu, X., Li, W.P., Wang, Z.Z., Zhang, Q., Duan, A.M. and Liang, X.Y. (2007) The influence of mechanical and thermal forcing by the Tibetan Plateau on Asian climate. *Journal of Hydrometeorology*, 8(4), 770–789. https://doi.org/10.1175/jhm609.1.

Wu, J. and Gao, X.J. (2013) A gridded daily observation dataset over China region and comparison with the other datasets. *Chinese Journal of Geophysics*, 56(4), 1102–1111 (in Chinese). https://doi.org/10.6038/cjg20130406.

Xin, X.G., Wu, T.W., Zhang, J., Yao, J.C. and Fang, Y.J. (2020) Comparison of CMIP6 and CMIP5 simulations of precipitation in China and the East Asian summer monsoon. *International Journal of Climatology*, 40(15), 6423–6440. https://doi.org/10.1002/joc.6590.

Xu, Z.X., Rhoades, A.M., Johansen, H., Ullrich, P.A. and Collins, W.D. (2018) An intercomparison of GCM and RCM dynamical downscaling for characterizing the hydroclimatology of California and Nevada. *Journal of Hydrometeorology*, 19(9), 1485–1506. https://doi.org/10.1175/jhm-d-17-0181.1.

Xu, Z.X., Vittorio, A.D., Zhang, J., Rhoades, A., Xin, X.G., Xu, H.M. and Xiao, C. (2021) Evaluating variable-resolution CESM over China and Western United States for use in water-energy nexus and impacts modeling. *Journal of Geophysical Research: Atmospheres*, 73(12), 1962–1970. https://doi.org/10.1029/2020jd034361.

Yan, Y.H., Zhu, C.W., Liu, B.Q. and Jiang, S. (2021) Annual cycle of East Asian precipitation simulated by CMIP6 models. *Atmosphere*, 12(1), 24. https://doi.org/10.3390/atmos12010024.

Zarzycki, C.M. and Jablonowski, C. (2014) A multidecadal simulation of Atlantic tropical cyclones using a variable-resolution global atmospheric general circulation model. *Journal of Advances in Modeling Earth Systems*, 6, 805–828. https://doi.org/10.1002/2014ms000352.

Zarzycki, C.M., Jablonowski, C., Thatcher, D.R. and Taylor, M.A. (2015) Effects of localized grid refinement on the general circulation and climatology in the Community Atmosphere Model. *Journal of Climate*, 28(7), 2777–2803. https://doi.org/10.1175/jcli-d-14-00599.1.

Zhang, G.J. and Mcfarlane, N.A. (1995) Sensitivity of climate simulations to the parameterization of cumulus convection in the Canadian climate centre general circulation model. *Atmosphere*, 33(3), 407–446. https://doi.org/10.1080/07055900.1995.9649539.

Zhang, J., Li, L., Zhou, T.J. and Xin, X.G. (2013) Evaluation of spring persistent rainfall over East Asia in CMIP3/CMIP5 AGCM simulations. *Advances in Atmospheric Sciences*, 30(6), 1587–1600. https://doi.org/10.1007/s00376-013-2139-7.

Zhang, J., Zhou, T., Yu, R.C. and Xin, X.G. (2009) Atmospheric water vapor transport and corresponding typical anomalous spring rainfall patterns in China. *Chinese Journal Atmospheric Sciences*, 33(1), 121–134 (in Chinese). https://doi.org/10.3878/j.issn.1006-9895.2009.01.11.

Zhang, L.X., Zhou, T.J., Klingaman, N.P., Wu, P.L. and Roberts, M. (2018) Effect of horizontal resolution on the representation of the global monsoon annual cycle in AGCMs. *Advances in Atmospheric Sciences*, 35(8), 1003–1020. https://doi.org/10.1007/s00376-018-7273-9.

Zhang, R.H. (2015) Natural and human-induced changes in summer climate over the East Asian monsoon region in the last half century: a review. *Advances in Climate Change Research*, 6(2), 131–140. https://doi.org/10.1016/j.accre.2015.09.009.

Zhou, T.J., Wu, B., Guo, Z., He, C., Zou, L.W., Chen, X.L., Zhang, L.X., Man, W.M., Li, P.X., Li, D.H., Yao, J.C., Huang, X., Zhang, W.X., Zuo, M., Lu, J.W. and Su, N. (2018) A review of East Asian summer monsoon simulation and projection: achievements and problems, opportunities and challenges. *Chinese Journal of Atmospheric Sciences*, 42(4), 902–934 (in Chinese). https://doi.org/10.3878/j.issn.1006-9895.1802.17306.

Zou, L.W., Zhou, T.J., Li, L. and Zhang, J. (2010) East China summer rainfall variability of 1958–2000: dynamical downscaling with a variable-resolution AGCM. *Journal of Climate*, 23(23), 6394–6408. https://doi.org/10.1175/2010jcli3689.1.

SUPPORTING INFORMATION

Additional supporting information can be found online in the Supporting Information section at the end of this article.

How to cite this article: Zhu, H., Zhang, J., Xu, Z., Di Vittorio, A. V., Xin, X., Xiao, C., & Li, Y. (2022). Advantages of a variable-resolution global climate model in reproducing the seasonal evolution of East Asian summer monsoon. *International Journal of Climatology*, 1–18. https://doi.org/10.1002/joc.7796